Transp Porous Med (2013) 96:39–62
DOI 10.1007/s11242-012-0072-3

Numerical Simulation of Diagenetic Alteration and Its Effect on Residual Gas in Tight Gas Sandstones

Maša Prodanović · Steven L. Bryant · J. Steven Davis

Received: 16 January 2012 / Accepted: 17 August 2012 / Published online: 19 September 2012

Abstract In this study, we numerically cemented a segmented X-ray microtomography image of a sandstone to understand changes to pore space connectivity, capillary control on gas, and water distributions, and ultimately production behavior in tight gas sandstone reservoirs. Level set method-based progressive quasi-static algorithm (a state-of-the-art direct simulation of capillarity-dominated fluid displacement) was used to find the gas/water configurations during drainage and imbibition cycles. Further, we account for gas–water interfacial tension changes using 1D burial history model based on available geologic data. We have found the displacement simulation method robust, and that diagenetic changes impart a significantly larger effect on gas trapping compared with interfacial tension changes.

Keywords Numerical cementation · Drainage and imbibition · X-ray images · Level set method · Burial history

1 Introduction

Unconventional gas resources, among which tight gas sandstones (TGS) represent about 50–70 % are predicted to be the dominant source for the US national gas supply in the next two decades (Miller and Shanley 2010; Byrnes and Cluff 2009). Tight gas sandstones are characterized by very low porosity, typically less than 10 %. The geometry of pore space at this porosity differs from conventional reservoir sandstones in some fundamental aspects: owing to diagenetic changes (cementation, partial dissolution, clay filling) the fluid pathways are significantly narrower, and some percentage of the fluid pathways are closed and disconnect the pore space. This profoundly affects permeability and other macroscale fluid properties

M. Prodanović (✉) · S. L. Bryant
Department of Petroleum and Geosystems Engineering, The University of Texas at Austin,
200 E. Dean Keeton, Stop C0300, Austin, TX 78712-1585, USA
e-mail: masha@ices.utexas.edu

J. S. Davis
Exxon Mobil Upstream Research Company, P.O. Box 2189, Houston, TX 77252-2189, USA

and is the reason for failure of predictive capabilities of conventional porosity–permeability relationships. Ultimately, this results in the inability to predict economic versus noneconomic intervals using standard formation evaluation tools and techniques.

High-resolution, three-dimensional, X-ray microtomography images of multiphase porous media have become widely available over the last decade (Flannery et al. 1987; Wildenschild et al. 2002). At the same time, several methods have been developed to both analyze the imaged pore space and calculate macroscopic flow properties (Øren and Bakke 2003; Turner 2007; Prodanović et al. 2007). The feedback loop between properties calculated by analyzing imaged porous materials (as well as sequences of images from a multiphase flow or a rock mechanics experiment) and laboratory measured properties has been commonly referred to as "digital rock laboratory." In this article, we isolate cementation and study its influence on the pore space and capillarity-dominated flow properties within the "digital rocks" framework.

The basis for our study is a 3D image of the solid and void space (the so-called binarized or segmented image) of a well-studied conventional sandstone sample. We numerically grow cement to create lower porosity models in the range of 6–20 %, the low end porosity similar to TGS porosities. We first investigate the influence of various numerical cementation modes on pore space connectivity using medial axis-based methods and pore–throat network analysis (Prodanović et al. 2007, 2006). We then use the binarized (segmented) image directly to estimate final multiphase (gas and water) saturations and distributions in low porosity sandstones using a novel drainage and imbibition numerical simulation technique that works directly in the imaged pore space. The numerical simulation uses a level set method-based progressive quasi-static (LSMPQS) algorithm (Prodanović and Bryant 2006) to track interface movement and position for the multi-phase gas–water system. The LSMPQS method is specifically designed for situations where the capillarity forces dominate viscosity and gravity and is robust with respect to the pore space geometry in both 2D and 3D simulations (Prodanović et al. 2010). LSMPQS has been validated against experiments in our previous study. The comparison includes the fluid displacement within single pores (Prodanović and Bryant 2006), and within a fracture where displacement experiment was directly imaged (Prodanović et al. 2010).

Finally, we look into the relative influence of diagenetic alteration (cementation) and interfacial tension changes over time on the residual gas saturation. Both diagenesis and interfacial tension are sensitive to pressure and temperature conditions. Thus, both will be impacted by the burial history of a rock–fluid system. Using the LSMPQS methodology, we simulate the multiphase drainage and imbibition behavior through a typical burial-exhumation cycle during which the parameters that control capillary behavior in the subsurface change continuously. These parameters include pore and pore throat dimensions (i.e., capillary radius) and interfacial tension (IFT, sensitive to changes in pressure and temperature). To simulate these changes, we follow the cementation scheme above and also back-calculate IFT changes over the geologic time using the estimated pressure–temperature paths from a 1D burial history model. Our simulation results show that cementation and compaction of the pore space have a first-order effect, while IFT changes are of secondary importance.

2 Methods

2.1 Image-based Pore Space Characterization

In order to perform a comprehensive comparison of cemented samples, we use a set of tools, which identifies a network of pores (openings) and throats (constrictions) using a segmented

image. Multiple approaches are available (Bakke and Øren 1997; Sheppard et al. 2006), and we used the methodology embedded within 3DMA-Rock software (Lindquist 2010; Prodanović et al. 2006). The segmented image is first processed to construct the medial axis (skeleton, (Lee et al. 1994)). The medial axis skeleton serves both as an easier way to visualize the pore space pathways (and their disconnections) and as a starting point for further analyses such as path tortuosity computation and throat finding. We then apply multiple throat-finding approaches (Lindquist and Venkatarangan 1999; Shin et al. 2005) that use the medial axis paths to search for cross sections or locally minimal areas. Using the throats found, the pore space is then divided into pores (Prodanović et al. 2006). The corresponding parameters, e.g., pore and throat areas, and coordination numbers, are also readily calculated, and these parameters form the basis for our comparison.

2.2 Numerical Cementation of Sandstone Samples

Øren et al. (2007) introduced process-based reconstruction of sandstones, now a fairly common method, (Mousavi and Bryant 2007; Motealleh and Bryant 2009; Torskaya et al. 2007) of generating sandstone samples based on numerical simulation of geologic processes. They start from a model disordered packing of spherical grains (where packing process mimics sedimentation), then make numerically compact and diagenetically alter them to various degrees. Uniform cement growth, for instance, can easily be simulated by modifying sphere radius. Preferential cement growth can be favored in pore throats (thus easily disconnecting the pore space) or pore bodies (where pore space remains connected at rather low porosities). Finally, pore lining, pore filling, and pore bridging clays can be numerically added in somewhat simplified form. Mousavi and Bryant (2007) use uniform cement overgrowth on a spherical packing, with a possibility of an outside part of the each sphere being ductile (soft) and redistributing itself on the pore space.

Unlike process-based reconstruction approaches described above, we do not use sphere packing as a starting point but an X-ray microtomography image of a sandstone sample. The original image has been segmented (or binarized), i.e., processed to define which voxels (numerical cells) belong to pore space and which to grain space. Image segmentation is a research topic on its own, and quality segmentation is very important to subsequent results of sample characterization and numerical modeling. In this article, however, our purpose is not to evaluate segmentation algorithms and we treat the segmented image as the ground truth. An interested reader is referred to a review article on the topic (Iassonov et al. 2009).

The sandstone image (approx. 20 % porosity) is already compacted and cemented, and provides us with a starting point to simulate further cementation to obtain a tight (low porosity) sandstone sample. As we have no knowledge of grain locations, we cannot manipulate sphere radius but can work with entire pore–grain interface. We implement a general cementation algorithm using the level set method (described below in more detail), and use both uniform and nonuniform cementation.

2.2.1 Level Set Method for Numerical Cementation

The level set method was initially introduced by Osher and Sethian (1988), and has gained application in numerous areas related to physical problems that can be modeled by moving interfaces (Sethian 1999; Osher and Fedkiw 2002). In the cementation application, the interface is the pore–grain surface in a porous medium that moves into the pore space (i.e., the grain space effectively grows, the pore space effectively shrinks) as cement is deposited on the surface. In another application (see Sect. 2.3), we use a level set method-based algorithm

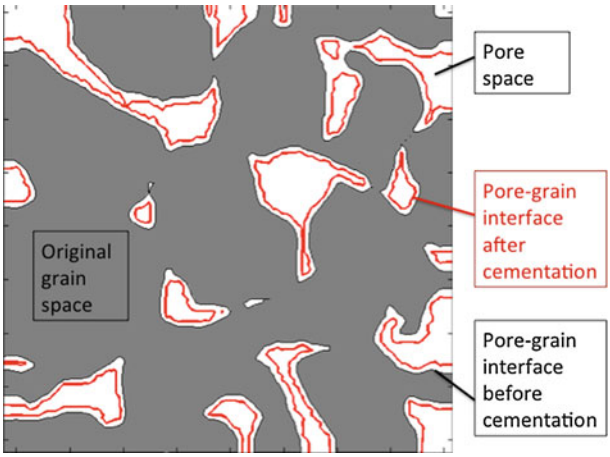

Fig. 1 Cementation procedure: the cross section of a sandstone sample showing original grain space in *gray*, and the pore space in *white*. After uniform cementation, pore–grain interface has moved to the new location inside the pore space. Note that some portion of the original pore space has disconnected in the process

to track fluid–fluid interface motion in a porous medium under the influence of capillary forces and pressure difference between the fluids.

The zero level set of a function ϕ is used to represent the position of interface at all times. In our case, $\phi < 0$ denotes wetting phase and $\phi > 0$ denotes nonwetting phase and solid grain together. The differentiation of $\phi = 0$ with respect to time and space gives the following:

$$\frac{\partial \phi}{\partial t} + F|\nabla \phi\,(\vec{x}(t), t)\,| = 0 \tag{1}$$

Equation (1) governs the evolution of function ϕ in space during a period of time, so that the interface of interest is at all times embedded as the zero level set. F is the interface movement speed, with the assumption of F normal to the interface.

2.2.2 Uniform Cementation

In uniform cement growth, we initialize the level set function as follows. All voxels within the solid phase are set to the positive distance to the closest pore voxel, and all voxels within the pore phase are set to the negative distance to the closest solid voxel. Thus, the pore–grain interface is represented by zero values of the level set function, $\phi = 0$. Uniform cement growth assumes that cement is deposited at the same rate at all grain surfaces, and as it is growing into the pore space (negative values of the level set function), the speed F in Eq. (1) set to a negative constant (e.g., Fig. 1). Note that when two "growing" grain interface touch, grains merge, and the interface locally disappears; the level set methodology handles such mergers with ease.

2.2.3 Nonuniform Cementation

In nonuniform, preferential cementation, the grain surfaces near throats (narrow parts of fluid pathways) are cemented at a lower speed than those neighboring pores (wider openings). This mimics the situation where in wider pore spaces the water flow of fluid is general

slower and presumably allows for more precipitation of cement. The local speed of cementation is a dynamic function of the local velocity field, among other parameters (Meakin and Tartakovsky 2009). Short of finding the velocity field (which would require an additional computationally demanding simulation), we note that the local flow speed depends on whether we are in a pore or throat. Thus, the local speed of cementation requires that in the pore space near a grain surface we know the distance to the local center of the pore space.

In order to determine the distances to the local centers of the pore space, we utilize medial axis analysis as follows. We first post-process the segmented image to find the medial axis (skeleton) of the pore space (see Sect. 2.1). The medial axis is a network of digitized paths that represents the centerline of the pore space. As it simplifies geometrically complicated pore space, it is commonly used for visualization, characterization or as a search tool in porous media. For each point of the pore space we then compute the distance from the closest medial axis point. We scale all of the distances 'd' by the maximum in the image, so that they all belong to [0,1] interval. Note that such defined distances will be highest (close to 1) at the edges of large pores (and thus far away from the middle of the pore space), and 0 at medial axis points (in the middle of the pore space). In very tight throats, the distance will also be close to 0.

We then use level set modeling to find the cemented pore–grain interface. We start from the level set function that is negative in the pore space and positive in the grain space. During cementation the interface between the pore and grain space (zero level set) will move into the pore space, i.e., against the gradient (and thus normal to the local interface) direction. We define the cementation speed F at each pore space point as $F(x) = -d(x)$, where $d(x)$ is local distance from the medial axis). The pore–grain interface is then exposed to the motion in the normal direction (away from the grain space) where the interface speed is set to F. Note that in the uniform cement case the speed was everywhere -1. Because the speed is 0 at the skeleton, the pore space will remain connected at lower porosities compared to uniform cementation. We exemplify the uniform versus pore throats filling cementation on a simple 3D sandstone pore example (see Figs. 2, 3).

2.3 Level Set Method Progressive Quasi-Static (LSMPQS) Algorithm for Multiphase Flow Simulation

In LSMPQS algorithm, F reflects the influence of difference between capillary pressure and fluid/fluid curvatures scaled by interfacial tension. We assume slow, quasi-static displacement of immiscible fluids, and at each stage of the simulation we assume the Young–Laplace equilibrium equation is valid:

$$P_c = P_{nw} - P_w = \sigma\kappa.$$

Thus, the interface between fluids, characterized by interfacial tension σ, curves with the mean curvature κ to accommodate capillary pressure P_c (difference between nonwetting, $P_{nw,}$ and wetting, $P_{w,}$ phase pressures).

2.3.1 Drainage

At the initial step of drainage, F is determined by:

$$F(\vec{x}, t) = a_0 \exp\left[f\left(1 - \frac{V(t)}{V_m}\right)\right] - b_0\,\kappa(\vec{x}, t) \tag{2}$$

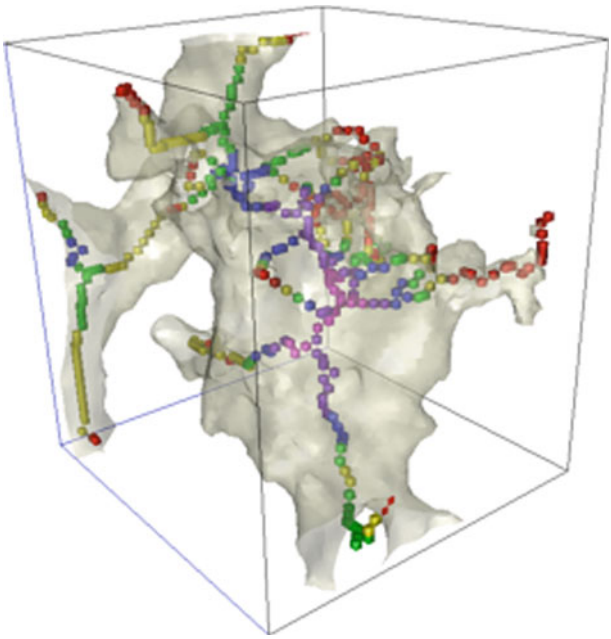

Fig. 2 A surface of a sandstone pore ($51 \times 50 \times 57$ voxels, extracted from a Berea image with voxel length $4.93\,\mu$m (Prodanović et al. 2007)) is shown transparent, and the medial axis voxels are shown in *color*. The *rainbow* coloring indicates how close is the medial axis voxel to the closest grain voxel (from *red*—1 voxel away to *violet*—10 voxels away)

The first term on the right hand side represent the influence of capillary pressure, where a_0 is a reference pressure, f is the dimensionless bulk modulus, and V_m and $V(t)$ are a target volume and the phase volume inside the boundary, respectively. The second term reflects the surface energy, where b_0 is the surface tension and $\kappa(\vec{x}, t)$ is twice the average curvature of the interface. At steady state, the fluid/fluid interface is stabilized, so that F is zero everywhere in the computational domain. Capillary pressure and surface tension are balanced under this condition.

After the initial stage, we increase the curvature by $\Delta\kappa$, and evaluate the following speed function

$$F(\vec{x}, t) = a_0 - b_0\,\kappa(\vec{x}, t) \tag{3}$$

to get the new steady state, at which the capillary pressure and surface tension are balanced again. That is, the non-trivial steady state solution of z Eq. (1) with F defined in Eq. (3) is the interface that at every point has a constant curvature:

$$\kappa = a_0/b_0 (= \mathrm{P_c}/\sigma) \tag{4}$$

Fluid configurations, such as fluid distribution and interface, can be easily computed: most advanced visualization software can identify and display zero (or any other) level set. Our implementation, shown in Sect. 3, produces a Geomview (http://www.geomview.org) file and is available within LSMPQS software (Prodanović 2010).

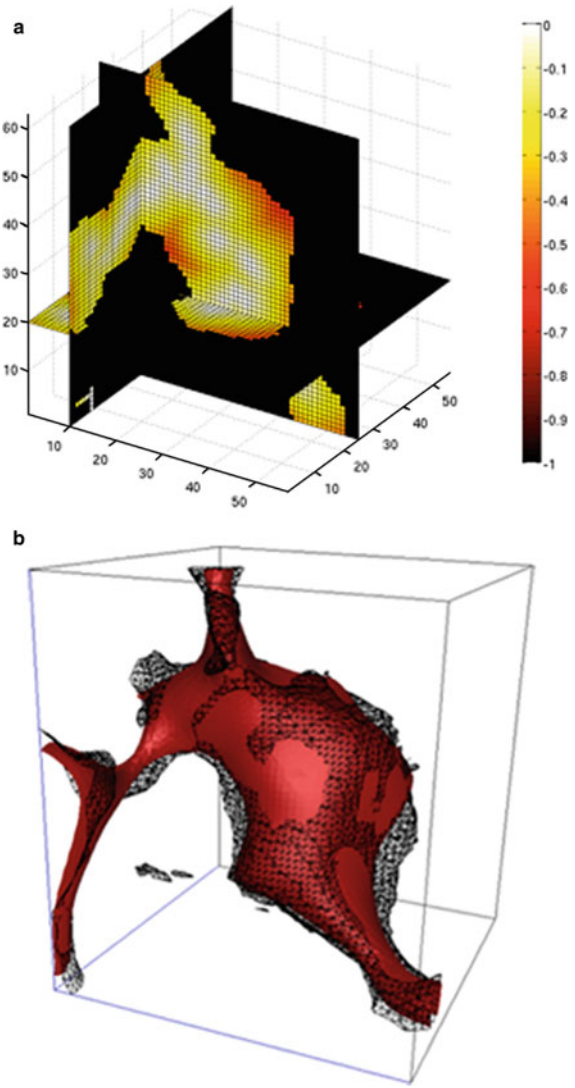

Fig. 3 **a** Speed function F to be used for pore throat filling cementation on the same Berea pore. The largest absolute values are near grain surfaces of wider pore spaces (decided on nontrivial 3D distances as explained in the text). Note that for the uniform cementation, speed F is the same everywhere. **b** Difference in the nonuniform cementation of the above pore (shown in *red*) and uniform cementation (shown as transparent *black mesh*) for approximately same resulting porosity. The surfaces neighboring large opening (middle of the pore) are cemented much more faster than those neighboring throats

2.3.2 Solid–fluid Contact

The boundary of the computational domain is defined by introducing the fixed level set function ψ (called 'mask'), where the pore–grain boundary is described by $\psi = 0$, and the level set function in the pore space satisfies $\phi((\vec{x}, t) \leq \psi$. We enforce the mask after every

step thus preventing the fluid/fluid interface entering into the grains. Furthermore, it results in a zero contact angle (without explicitly solving for it).

2.3.3 Imbibition

Imbibition is initialized with a chosen drainage endpoint (and associated mean curvature, κ), and at each subsequent step decreases prescribed curvature further (Eq. (3)).

2.3.4 Interfacial Tension (IFT) Changes

Any simulation can be a sequence of drainage and imbibition events as necessary. As we conceptually start from Young–Laplace equation (at each stage, the product of interfacial tension and mean curvature is constant), a reduction in IFT (assuming unchanged capillary pressure) is equivalent to capillary increase in mean curvature of the interface between phases and thus a drainage event.

2.4 Interfacial Tension (IFT) Changes Over Geologic Time

Interfacial tension correlates to the densities of immiscible fluids across the interface between them Firoozabadi and Ramey (1988). Fluid densities in the subsurface should be sensitive to both compositional changes and pressure and temperature changes through geologic time. Thus, it is expected that interfacial tension will change through the history of a multiphase fluid charged porous rock. In order to calculate IFT through time we used the following correlation developed by Firoozabadi and Ramey (1988) for the relationship between IFT ($\sigma_{\text{water}-\text{HC}}$) of a water-hydrocarbon system and the density difference between the two immiscible phases ($\rho_{\text{water}-\text{HC}}$):

$$\sigma_{\text{water}-\text{HC}} = \left[\Delta\rho_{\text{water}-\text{HC}} \left(T_{pr}^{HC}\right)^{-0.3125} \tau\right] \tag{5}$$

where is T_{pr}^{HC} the pseudo-reduced temperature of the hydrocarbon phase, and

$$\tau = e^{\left[0.09125 \ln(\Delta\rho_{\text{water}-\text{HC}})^2 - 0.53833 \ln(\Delta\rho_{\text{water}-\text{HC}}) + 1.227328\right]} \tag{6}$$

Brine and methane densities depend on fluid composition, pressure, and temperature. We used the Bennedict–Webb–Rubin–Starling (BWRS) equation of state (Starling 1973; Benedict et al. 1940; Benedict 1942) to calculate the subsurface fluid densities used in the Firoozabadi–Ramey relationship for IFT. Relevant inputs to the BWRS calculation include water and gas compositional data from a typical tight gas accumulation in the western United States, as well as pressures and temperatures estimated from a 1D burial history model for that basin (Yurewicz et al. 2005). Water composition (total dissolved solids 14,000 ppm) and gas composition (86.4 % methane, 5.6 % ethane, 1.5 % propane, 4.6 % carbon dioxide, and less than 1 % other hydrocarbon and non-hydrocarbon phases) was held constant, but pressure and temperatures varied through time according to the 1D burial history model.

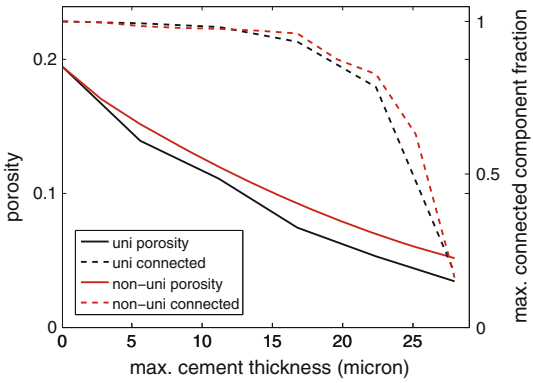

Fig. 4 Porosity dependence of (approximate) the thickness of cement (in microns) grown both uniformly and nonuniformly on the pore–grain surface of the Castlegate sandstone image. *Dashed lines* show connected fraction of the pore space for each image, for uniform and nonuniform cementation. In case of the nonuniform cementation, the thickness is not the same at all surfaces, and we plot against maximum possible thickness in the image

3 Results and Discussion

We use a publicly available Castlegate sandstone microtomography image (image downloaded from Pore Network Comparison Forum.[1] As mentioned previously, the image posted has been previously segmented (binarized). We investigated with a 256^3 voxel subsample of the original 512^3 voxel image with a voxel edge length of $5.6\,\mu$m.

We first present the effect cementation (described in Sect. 2.2) has on the pore space using pore–throat network characterization in Sect. 3.1, then proceed to drainage and imbibition simulation in Sects. 3.2 and 3.3 with the objectives of studying the influence of cementation and changing interfacial tension on residual fluids in the pore space.

3.1 The Effect of Uniform and Nonuniform Cementation on Pore space Geometry

As we grow cement (i.e., move the pore–grain interface into the pore space with constant velocity using level set methodology outlined in Sect. 2), we record the resulting porosity, as well as the fraction of the pore space occupied by the largest connected component (Fig. 4). Nonuniform cementation tends to have higher porosity and connectivity for the same maximal cement thickness. Sharp drop in the connected fraction values indicates that the pore space is not connected across the sample (in any coordinate direction).

For comparison, we selected samples of 20 % (original), 15, 10, and 7 % porosity. Note that the samples with porosity below 7 % are disconnected, i.e., there is no connected path through the pore space across the sample (in any direction). We show examples of grain surface and the skeleton of the pore space (medial axis, produced and post-processed using 3DMA-Rock) for selected samples (Figs. 5, 6). Medial axis voxels in both figures are colored according to the distance to the closest grain. Thus, tightening of the pore space for the sample with porosity 10 % is obvious by uniform "color shift" to red in Fig. 5b, d.

Nonuniform and uniform cementation have quite a different effect on the sample of similar porosities. As is visible from Fig. 6, nonuniformly cemented sample of porosity 11 % has less open pathways and overall less connectivity than the uniformly connected sample. The distances of the skeleton voxels to the closest grain voxel are more evenly distributed and not as narrow as for the 10 % porosity sample in Fig. 5.

[1] http://xct.anu.edu.au/network_comparison/, last accessed September 1, 2012.

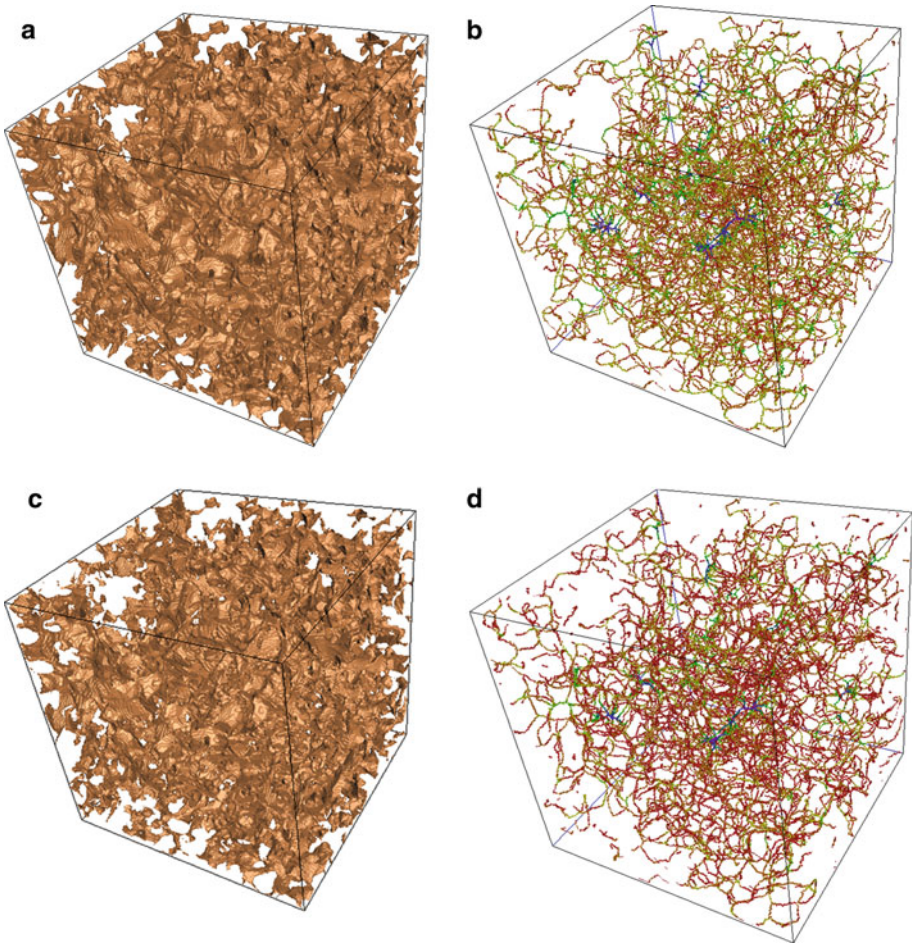

Fig. 5 Pore grain surfaces (**a**, **c**) and the pore space skeletons (**b**, **d**) for the original sample and the uniformly cemented sample of porosity 10 %. The skeleton voxels are colored according to their distance to the grain surface, similar to Fig. 2

We created pore–throat network for each of the images using 3DMA-Rock software. Uniform cementation results in a shift to smaller pore volumes (Fig. 7a). Nonuniform cementation affects pores and throats differently, and fills in wider spaces more quickly. This results in a slightly more "even" distribution of pore volumes (Fig. 7b). With increasing cement thickness, more and more pores get disconnected, but they also get smaller. As we report the fraction of the pore volume (Fig. 7), or throat areas (Fig. 8) that each bin occupies, the "spike" in small sizes with tighter media is not as prominent as it would be if number frequency were reported. The effect of cementation on connectivity (visualized using medial axis) can be seen by the drop in pore coordination number distributions (i.e., number of other pores to which each pore in the network is connected) provided in Fig. 9. Nonuniform porosity, again, is proven to disconnect the pore space more with a much larger fraction of pore volume belonging to pores of low coordination number 3.

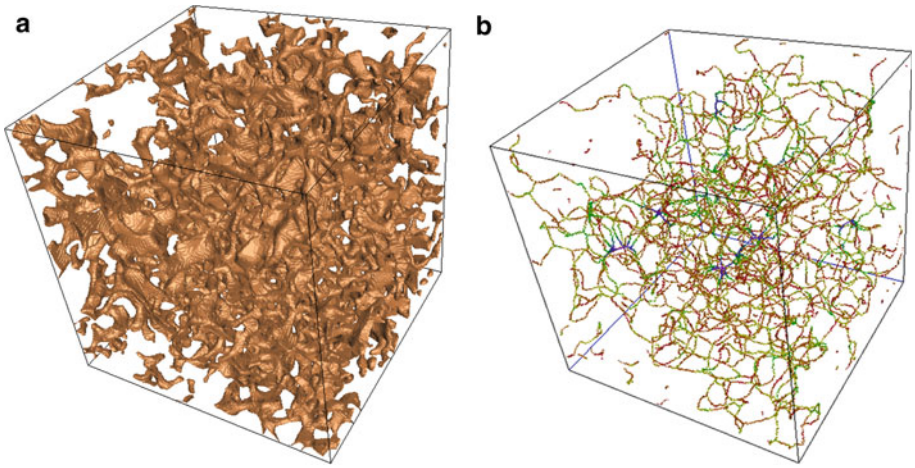

Fig. 6 Pore grain surface (**a**) and the pore space skeleton (**b**) for nonuniformly cemented sample of porosity 11 %

3.2 The Effect of Cementation on Residual Fluid Saturation and Spatial Distribution

Figure 10 shows (only) gas configuration at the end of LSMPQS drainage simulation for the original sandstone sample, and a selected uniformly cemented sample. Tightening of the pore spaces is shown by "thinning" of red areas that represent fluid meniscus. Residual water phase is complementary to the gas configurations (Fig. 11).

The capillary-pressure saturation curve for entire drainage and imbibition simulation is shown on Fig. 12. Residual wetting (water) saturation at drainage (Fig. 11) increases from 0.25 to 0.31 with porosity reduction from 20 to 10 %, whereas residual gas saturations at imbibition increase nearly twofold (from 0.3 to 0.57, for visualization see Fig. 13) for the same porosity reduction. We were unable to perform a reliable simulation in a cemented sample of porosity 7 % with the resolution of the (cemented) image: most pore spaces were only slightly larger than one voxel (numerical cell) across.

On the same capillary pressure–saturation plot (Fig. 12), we also see comparison with the nonuniformly cemented sample of porosity 11 %. There is more wetting phase trapping than for any other samples (original, uniformly cemented ones), the percolation threshold is close to that of uniformly cemented sample of 15 % (and much lower than for uniformly cemented sample of 10 %), and there is also much less residual trapping of nonwetting (gas) phase. For visualization of both residual water and residual gas phases, see Fig. 14. All these observations are consistent with the fact that nonuniform cementation (as implemented here, Sect. 2.2.3) is "evening" out the pore space width between pores and throats (aspect ratio is much less than for uniform cementation). Uniform cementation adds the same thickness of the cement everywhere, and this has disproportionate effect on throats (narrow pore spaces) than it has on pores (wider pore spaces). Figure 15 shows a close -up view that clarifies why cemented samples have higher relative residual gas phase fraction: relatively small amount of imbibing water can easily snap off nonwetting phase (that tends to be in the middle of the pore space) in tightened pore spaces. Note that level set-based modeling is ideal for studying this phenomenon.

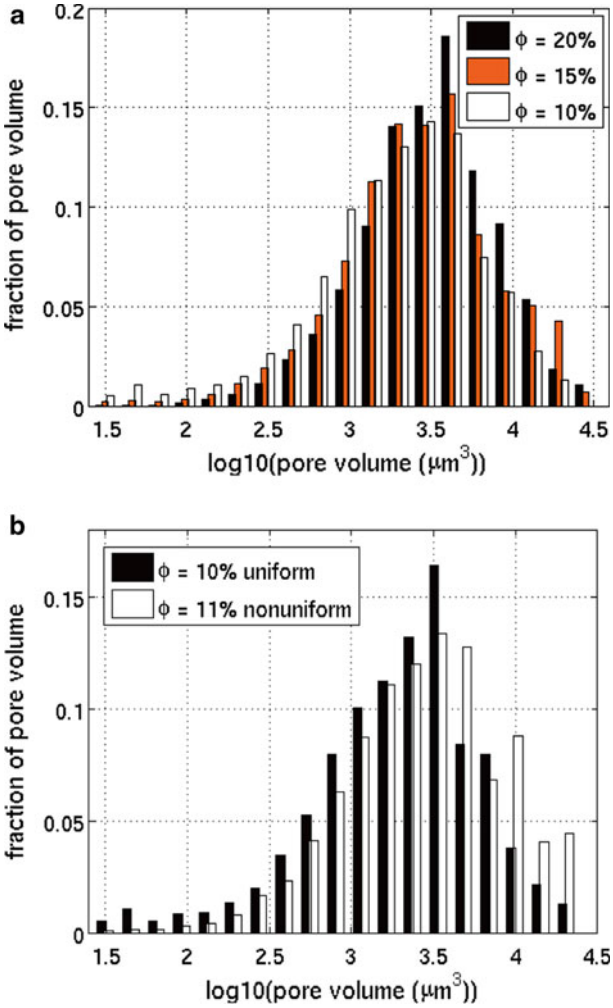

Fig. 7 Pore volume comparison for the selected **a** uniformly cemented samples of different porosities; **b** uniformly and nonuniformly cemented samples of similar porosity. Samples are identified by their porosity. Note that for each bin, we report fraction of total pore volume for all the pores belonging to the bin occupied rather than their total number or frequency

3.3 The Effect of Interfacial Tension Changes Over Geologic Time

IFT changes computed from a 1D burial model by Yurewicz et al. (2005) for a typical tight gas basin in the western USA are shown in Figs. 16 and 17. The interfacial tension follows the pressure and temperature changes associated with burial, initially decreasing during burial (∼80–20 Ma), then increasing during exhumation (20–0 Ma). Rapid IFT changes between 65 Ma and 60 Ma reflect subsidence, uplift, and exhumation during the Laramide Orogeny. The cycle with the largest number of imbibition to drainage (and back) changes is in dark blue, and we will use that cycle to investigate the effect of relative IFT changes on residual fluid distributions.

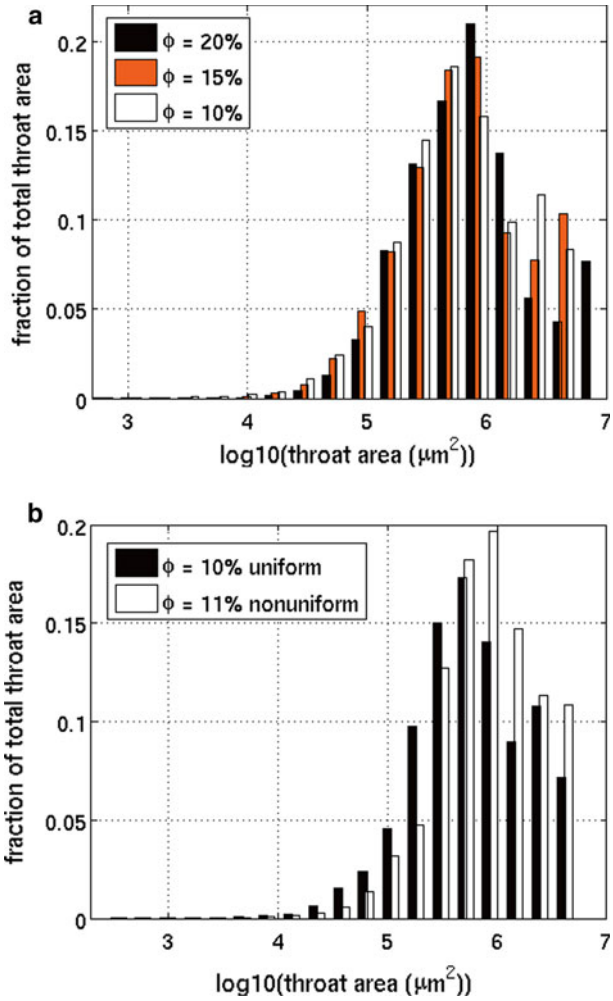

Fig. 8 Throat area comparison for the selected **a** uniformly cemented samples of different porosities; **b** uniformly and nonuniformly cemented samples of similar porosity. For each bin, we report fraction of total throat area for all the throats belonging to the bin, rather than their total number frequency

Note that the fluid–fluid interface resulting from any step of LSMPQS simulation is a function of the ratio of capillary pressure and interfacial terms, rather than their individual values. In simulation, interfacial tension term b_0 is kept constant, and in absolute value on the order of the length of each numerical cell in simulation (this is for numerical stability, and minimizing simulation time: this term affects the choice of time-step). Therefore, for simulation purposes, we compute relative interfacial changes (shown in Fig. 18) corresponding to IFT changes in the dark blue cycle shown in Fig. 19.

We implemented the IFT changes for the two later drainage cycle points for the uniformly cemented sample of porosity 10 %. Note that the IFT changes are equivalent to a sequence of imbibitions (I) and drainages (D). Given not so large relative differences in the corresponding capillary pressure input into LSMPQS simulation, the $P_c - S_w$ (capillary pressure vs.

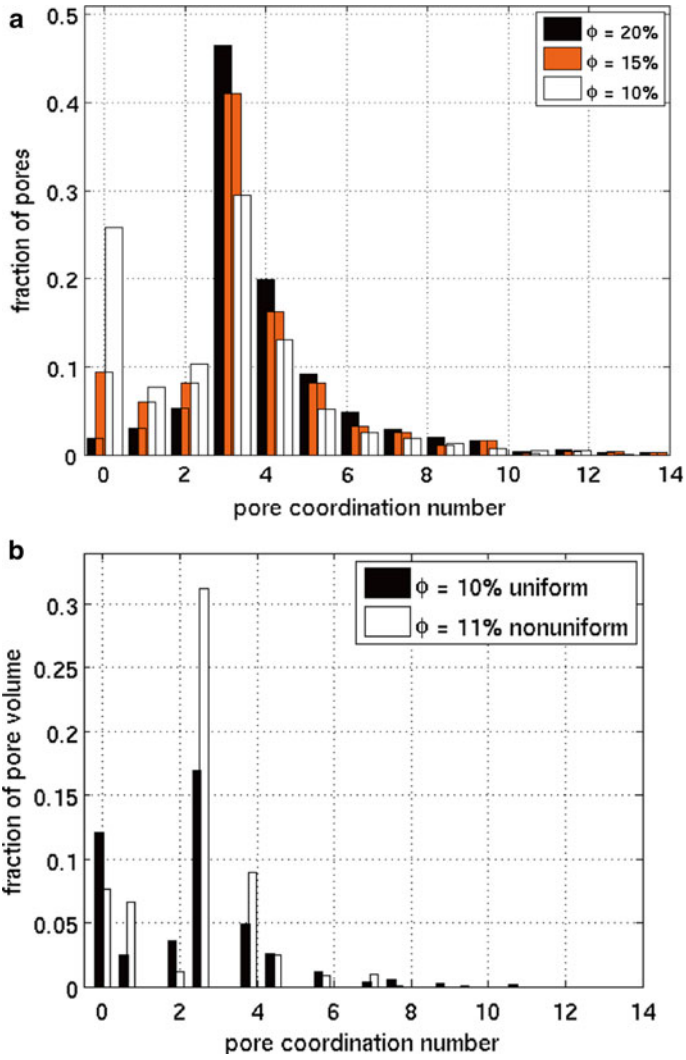

Fig. 9 Pore coordination number comparison for the selected (**a**) uniformly cemented samples of different porosities; (**b**) uniformly and nonuniformly cemented samples of similar porosity

water saturation) curves for these two cycles shown in Fig. 19 are rather difficult to follow as most points are on top of each other. At the end of both prescribed cycles, trapped gas phase is, however, observed, and it occurs at a higher effective capillary pressure than for the "regular" imbibition (identified by point A in the figure). The trapped fluids' configurations show that interfacial tension changes induce more irreversible displacement changes (i.e., more trapping). The trapped gas is also in different spatial positions for the two prescribed cycles and also different from the trapped configuration for the point A (not shown). The effect of more trapping, however, due to the interfacial changes, is much smaller in scale than that due to cementation shown earlier.

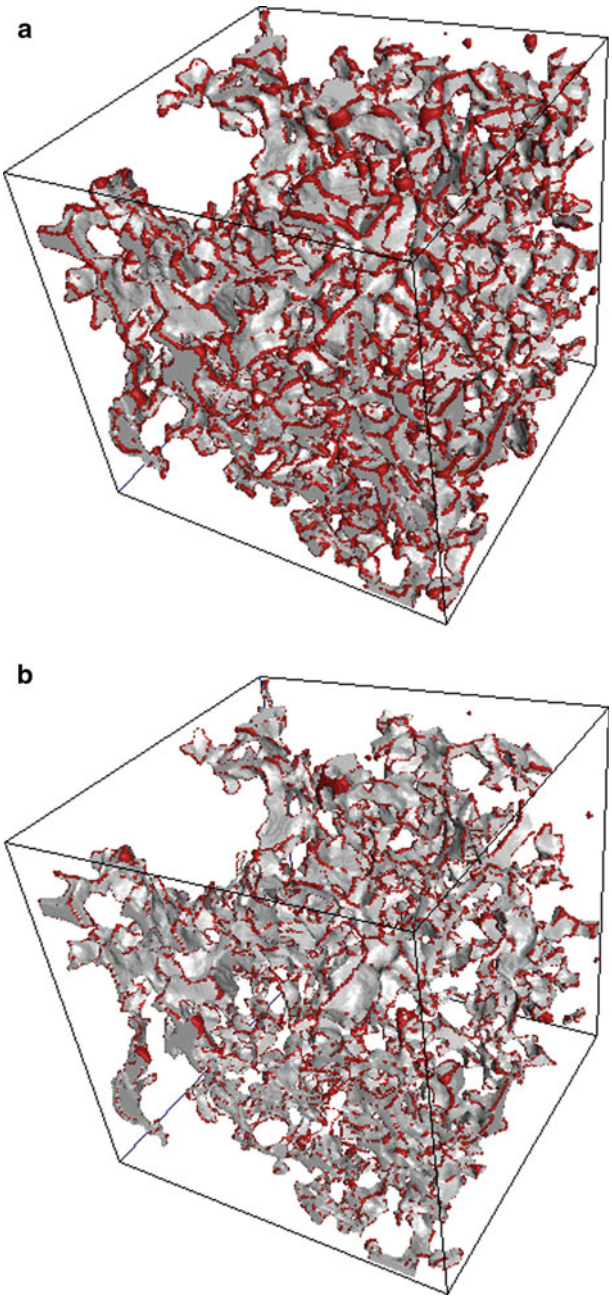

Fig. 10 Gas configuration surface (gas–solid contact is shown in *gray,* gas–water contact is shown in *red*) at the drainage endpoint for **a** original sandstone image, with porosity 20 %; and **b** uniformly cemented sample with 10 % porosity

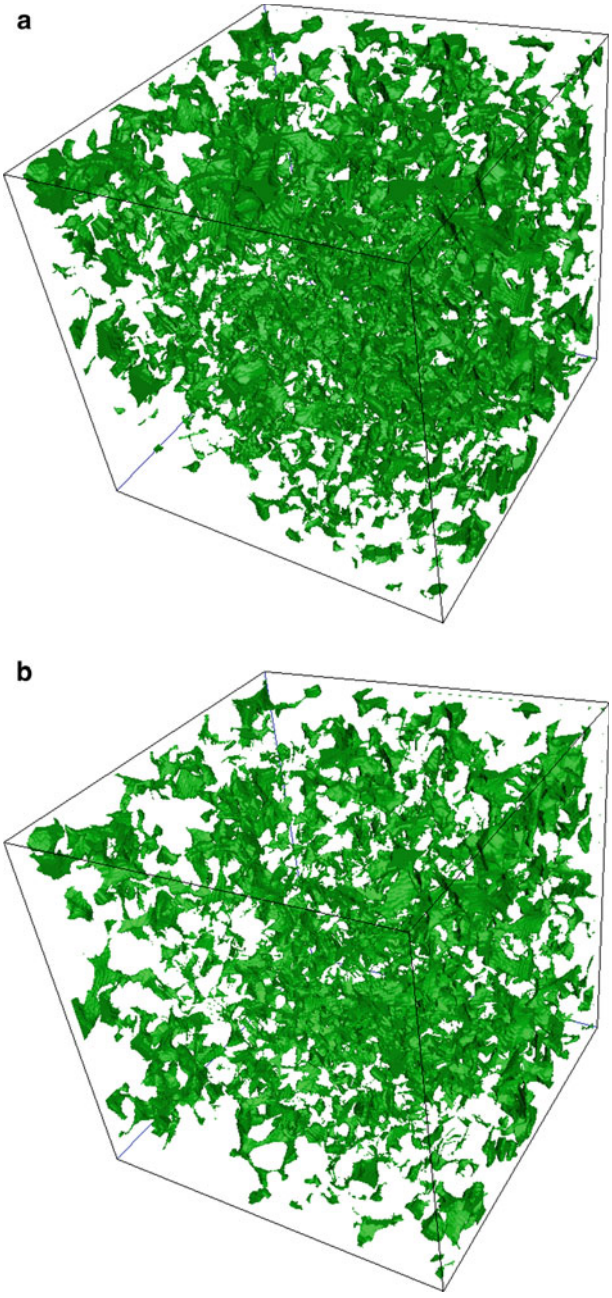

Fig. 11 Residual water configuration surface at the drainage endpoint for **a** original sandstone image, with porosity 20 % and residual saturation 0.25; and **b** uniformly cemented sample with 10 % porosity and residual saturation 0.31

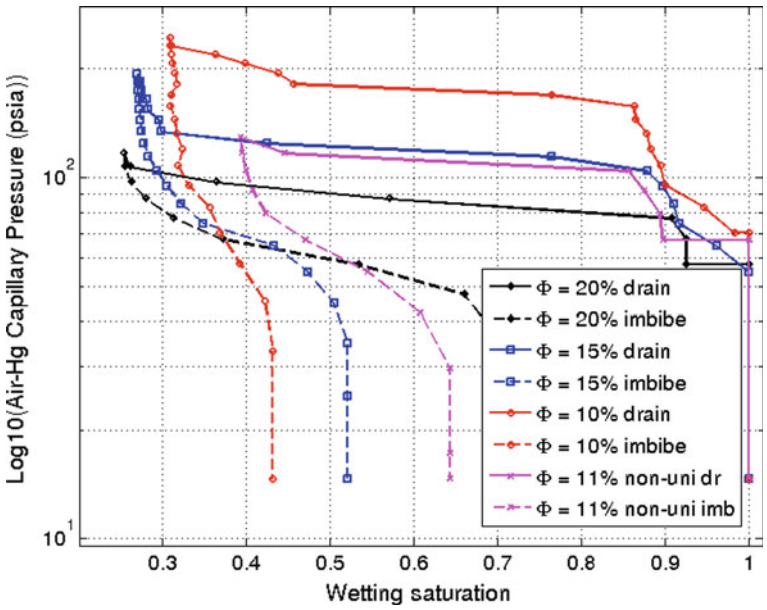

Fig. 12 Capillary pressure curves for drainage and imbibition in the original sandstone image (porosity 20 %); two uniformly cemented samples of porosity 15 and 10 %; and a nonuniformly cemented sample of porosity 11 %. Note that the LSMPQS simulation computes mean curvature—saturation curves, and the curvature values were scaled using air–water interfacial tension

4 Summary and Conclusions

Motivation for this study was to better understand capillary control on gas and water distributions, and ultimately production behavior in tight gas reservoirs, as well as estimate the predictive capability of the state-of-the-art direct simulation of capillarity-dominated fluid displacement.

We numerically investigated the influence of cementation of intergranular pore spaces on the fluid displacement: with tightening of the pore space, capillarity becomes more and more important. Further, having the access to appropriate data, we asked the questions: do changes in gas–water interfacial tension after reservoir charge alter the configuration of gas phase, and if so, what is the relative influence in comparison with diagenetic changes?

Pore scale, LSMPQS simulations in complex porous media akin to those in nature are found to be the key in understanding capillary control on gas and water distributions. Residual water and residual gas saturations increase with increasing cement (i.e., decrease in porosity and related connectivity, which is also observed in experiments) as well as because of the interfacial tension changes. Cementation (or changing the porosity), however, has much larger effect: a small amount of imbibing water can trap a relatively large amount of gas leading to high residual saturations. These saturations are similar to those observed in experiments (Byrnes and Cluff 2009). Intergranular (matrix) porosity modeled in this study, however, cannot fully explain the behavior of tight gas sandstone experiments: microporosity (with pore spaces less than the micron pore sizes captured by X-ray tomography) needs to be added and connected to the intergranular pore spaces so that very high capillary pressures

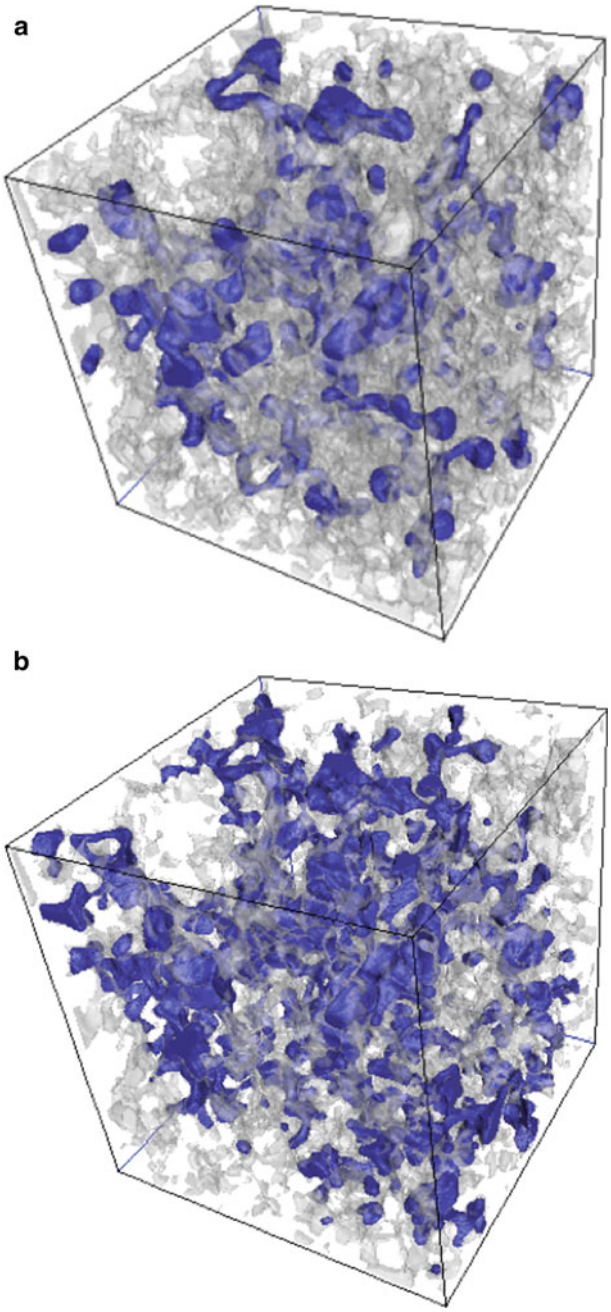

Fig. 13 Visualization of trapped gas (*blue*) in the pore space (pore–grain surface in transparent *gray*) for **a** original sandstone image with porosity 20 % and residual fraction 0.3; and **b** uniformly cemented sample with 10 % porosity and residual fraction 0.57

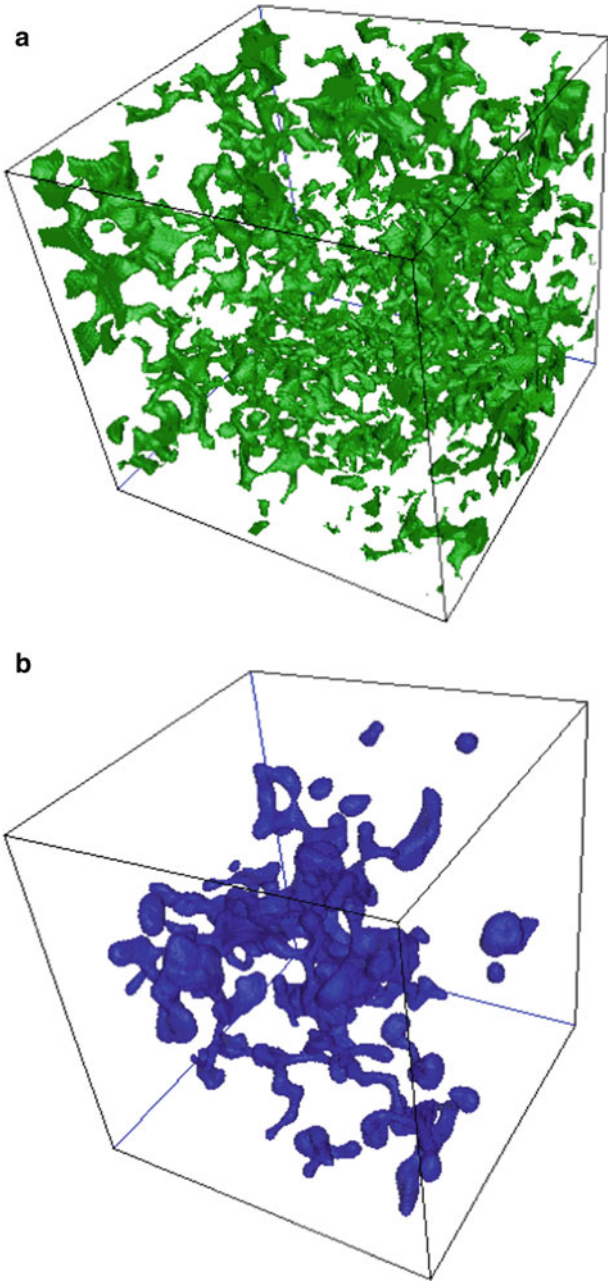

Fig. 14 **a** Residual wetting (water) phase at the end of drainage, fraction 0.39; and **b** residual nonwetting (gas) phase at the end of imbibition, fraction 0.36, for nonuniformly cemented sample of 11 % porosity

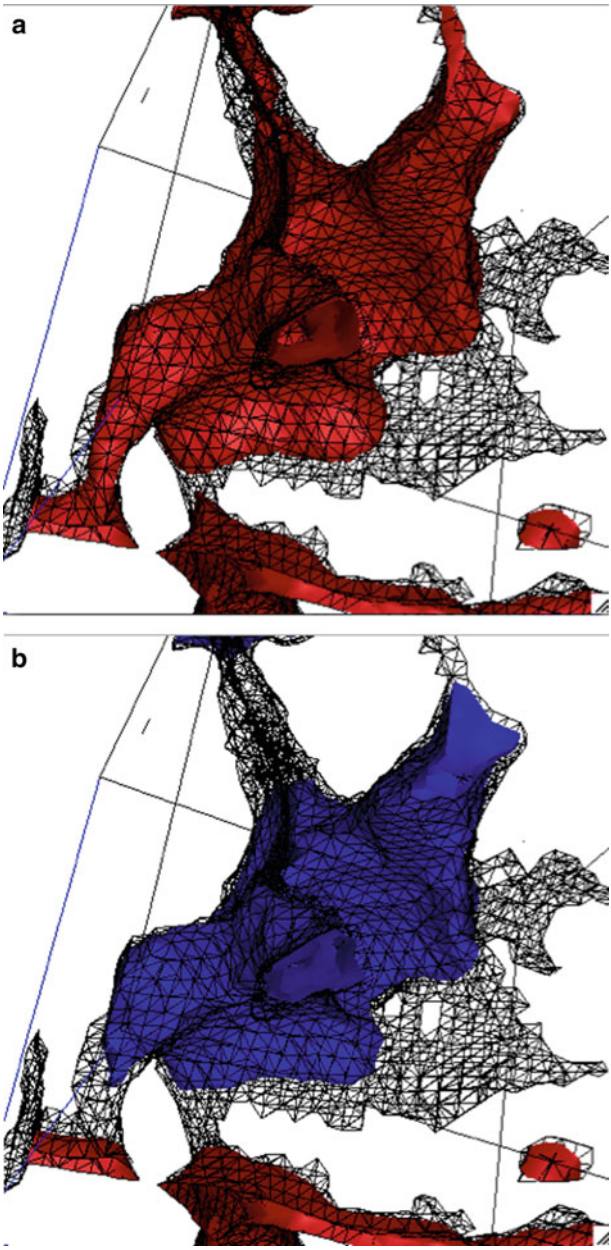

Fig. 15 Tightened pore spaces make it easy for a small amount of imbibing water to make contact and snap off the gas blob: this is a coordinated event in multiple throats. **a** Subvolume of the (uniformly) cemented sandstone pore space (pore grain surfaces are shown as a *triangle mesh*) with gas phase connected to the outlet (in *red*). Note that water phase is not shown and is filling the remainder of the pore space; **b** the same pore space at the next imbibition step with the trapped gas phase shown in *blue* (and the gas phase connected to the outlet still in *red*). Snap off has happened in three throats

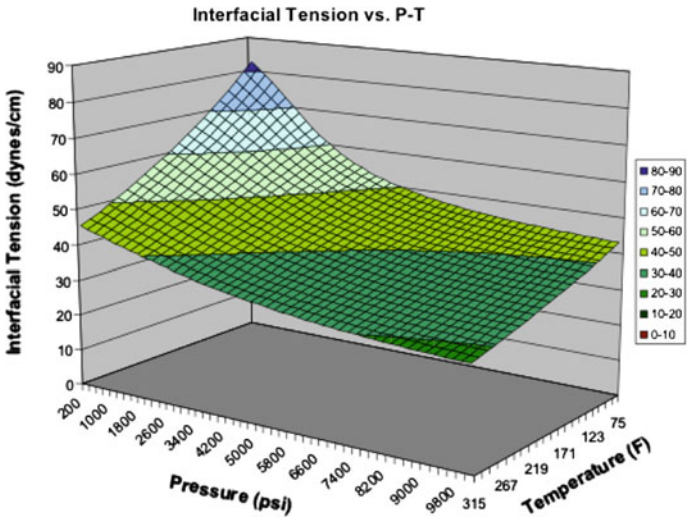

Fig. 16 Interfacial tension as a function of pressure and temperature calculated for water and hydrocarbon compositions described in Sect. 2.4

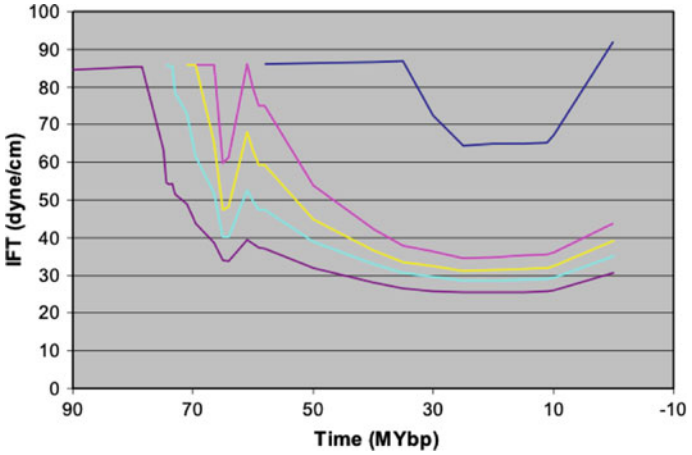

Fig. 17 Computed interfacial changes over geologic time based on the 1D burial history model presented in Yurewicz et al. (2005). *Different lines* represent different layers in the model

observed in experiments can be simulated. This requires multiscale methods, and we have started investigating them (Mehmani et al. 2011).

We have found that changes in gas–water interfacial tension (as calculated from available data) after reservoir charge alter the pore scale fluid configuration, and as fluids effectively go through a cycle of drainage and imbibition displacements, there is more gas trapping. We have found, however, that diagenetic changes impart a significantly larger effect on gas trapping compared with IFT changes. In our simulation of IFT changes, we have used a sample of fixed porosity. In reality, IFT and diagenetic changes are simultaneous, and often compete, but that does not change our conclusion on the relative comparison.

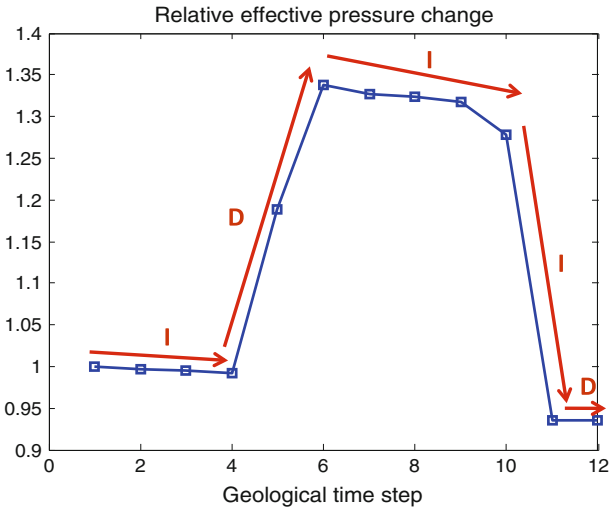

Fig. 18 Relative changes in capillary pressure relative to the starting point 60 million years ago. Effective imbibition (I) and drainage (D) sections of the IFT cycle are identified. The ending point is 30 million years ago

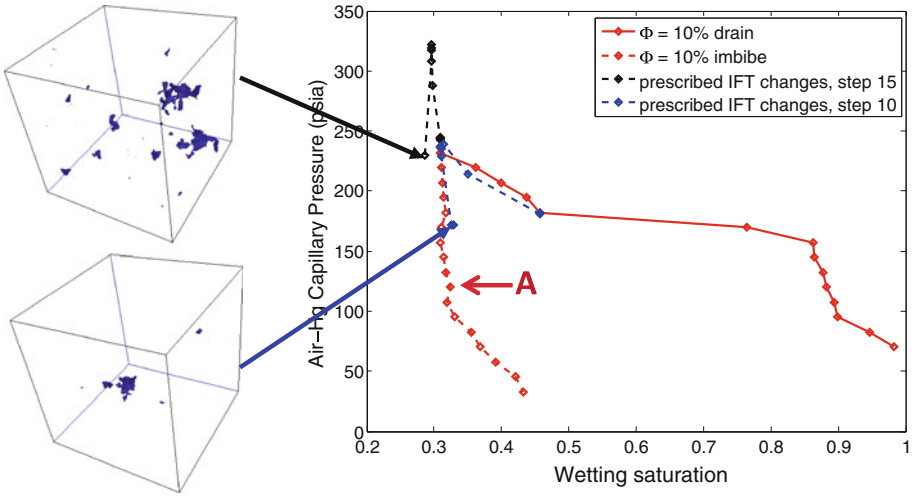

Fig. 19 Comparison of regular drainage/imbibition and the prescribed cycle schedule starting from two different drainage endpoints. The point identified by A is the first stage in "regular" imbibition where nonwetting phase trapping is observed. The trapped gas phase configurations (in *blue*) for the two endpoints of drainage are shown on the *left*

LSMPQS simulation is robust in replicating capillary behavior, allows significant sensitivity testing, and is quicker than physical experiments in tight reservoirs. It provides insight into small scale mechanisms. Like the most pore-scale investigations, simulation caveats include small sample size and difficulty in upscaling.

Acknowledgments This study has been supported by Exxon Mobil Upstream Research Company, Houston, TX. We gratefully acknowledge the permission granted by Exxon Mobil in allowing us to publish the results of this study.

References

Bakke, S., Øren, P.-E.: 3-D pore-scale modelling of sandstones and flow simulations in the pore networks. SPE J. **2**(2), 136–149 (1997)

Benedict, M.: An empirical equation for thermodynamic properties of light hydrocarbons and their mixtures II mixtures of methane, ethane, propane, and *n*-butane. J. Chem. Phys. **10**, 747 (1942)

Benedict, M., Webb, G.B., Rubin, L.C.: An empirical equation for thermodynamic properties of light hydrocarbons and their mixtures I methane, ethane, propane and *n*-butane. J. Chem. Phys. **8**, 334 (1940)

Byrnes, A.P., Cluff, R.M.: Analysis of Critical Permeablity, Capillary Pressure and Electrical Properties for Mesaverde Tight Gas Sandstones from Western U.S. Basins, U.S. Department of Energy. Available at: http://www.kgs.ku.edu/mesaverde/reports.html (2009)

Firoozabadi, A.F., Ramey, H.J., Jr.: Surface tension of water-hydrocarbon systems at reservoir conditions. J. Can. Petrol. Technol. **27**, 41–48 (1988)

Flannery, B.P., et al.: Three-dimensional X-ray microtomography. Science **237**(4821), 1439–1444 (1987)

Iassonov, P., Gebrenegus, T., Tuller, M.: Segmentation of X-ray computed tomography images of porous materials: a crucial step for characterization and quantitative analysis of pore structures. Water Resour. Res. **45**(9), W09415, 12pp (2009)

Lee, T.-C., Kashyap, R.L., Chu, C.-N.: Building skeleton models via 3-D medial surface axis thinning algorithms. CVGIP: Graph. Models Image Process. **56**, 462–478 (1994)

Lindquist, W.B.: 3DMA-Rock, a software package for automated analysis of rock pore structure in 3D computed microtomography images. http://www.ams.sunysb.edu/~lindquis/3dma/3dma_rock/3dma_rock.html. Accessed 31 January 2010

Lindquist, W.B., Venkatarangan, A.B.: Investigating 3D geometry of porous media from high resolution images. Phys. Chem. Earth A **25**, 593–599 (1999)

Meakin, P., Tartakovsky, A.M.: Modeling and simulation of pore-scale multiphase fluid flow and reactive transport in fractured and porous media. Rev. Geophys. **47**(3), RG3002, 47pp (2009)

Mehmani, A., et al.: The effect of microporosity on transport properties in tight reservoirs. In: SPE Americas Unconventional Gas Conference and Exhibition. Society of Petroleum Engineers (2011)

Miller, M., Shanley, K.: Petrophysics in tight gas reservoirs—key challenges still remain. Lead. Edge **29**(12), 1464–1469 (2010)

Motealleh, S., Bryant, S.: Quantitative mechanism for permeability reduction by small water saturation in tight-gas sandstones. SPE J. **14**(2) (2009)

Mousavi, M., Bryant, S.: Geometric models of porosity reduction mechanisms in tight gas sands. In: Proceedings of Rocky Mountain Oil & Gas Technology Symposium (2007)

Øren, P.-E., Bakke, S.: Reconstruction of Berea sandstone and pore-scale modelling of wettability effects. J. Petrol. Sci. Eng. **39**(3–4), 177–199 (2003)

Øren, P.-E., Bakke, S., Held, R.: Direct pore-scale computation of material and transport properties for North Sea reservoir rocks. Water Resour. Res. **43**, 11 (2007)

Osher, S., Sethian, J.A.: Fronts propagating with curvature–dependent speed: Algorithms based on Hamilton-Jacobi formulations. J. Comput. Phys. **79**(1), 12–49 (1988)

Osher, S.J., Fedkiw, R.P.: Level Set Methods and Dynamic Implicit Surfaces, 1st edn. Springer, Berlin (2002)

Prodanović, M.: Level Set Method based Progressive Quasi-Static (LSMPQS) software.http://users.ices.utexas.edu/~masha/lsmpqs/index.html. Accessed 30 January 2010

Prodanović, M., Bryant, S.: A level set method for determining critical curvatures for drainage and imbibition. J. Colloid Interface Sci. **304**(2), 442–458 (2006)

Prodanović, M., Lindquist, W.B., Seright, R.S.: Porous structure and fluid partitioning in polyethylene cores from 3D X-ray microtomographic imaging. J. Colloid Interface Sci. **298**(1), 282–297 (2006)

Prodanović, M., Lindquist, W.B., Seright, R.S.: 3D image-based characterization of fluid displacement in a Berea core. Adv. Water Resour. **30**(2), 214–226 (2007)

Prodanović, M., Bryant, S., Karpyn, Z.: Investigating matrix-fracture transfer via a level set method for drainage and imbibition. In: SPE Annual Technical Conference and Exhibition (2008)

Prodanović, M., Bryant, S., Karpyn, Z.: Investigating matrix/fracture transfer via a level set method for drainage and imbibition. SPE J. **15**(1) (2010)

Sethian, J.A.: Level Set Methods and Fast Marching Methods: Evolving Interfaces in Computational Geometry, Fluid Mechanics, Computer Vision, and Materials Science, 2nd edn. Cambridge University Press (1999)

Sheppard, A.P., et al.: Analysis of rock microstructure using high resolution X-ray tomography. In: Proceedings of the International Symposium of the Society of Core Analysts. International Symposium of the Society of Core Analysts. Trondheim, Norway, SCA, pp. 2006–2026 (2006)

Shin, H., et al.: Analysis of the vesicular structure of basalts. Comput. Geosci. **31**, 473–487 (2005)

Starling, K.E.: Fluid Thermodynamic Properties for Light Petroleum Systems. Gulf Publishing Co., Houston (1973)

Torskaya, T., Jin, G., Torres-Verdin, C.: Pore-level analysis of the relationship between porosity, irreducible water saturation, and permeability of clastic rocks. In: Proceedings of SPE Annual Technical Conference and Exhibition (2007)

Turner, M.L., et al.: Three-dimensional imaging of multiphase flow in porous media. Phys. A: Stat. Mech. Appl. **339**(1–2), 166–172 (2004)

Wildenschild, D., et al.: Using X-ray computed tomography in hydrology:systems, resolutions, and limitations. J. Hydrol. **267**(3–4), 285–297 (2002)

Yurewicz, D.A., et al.: Controls on gas and water distribution, mesaverde basin-centered gas play, Piceance Basin, Colorado. In: Cumella, S.P., Shanley, K.W., Camp, W.K. (eds.) Understanding, Exploring, and Developing Tight-Gas Sands—2005 Vail Hedberg Conference, pp. 105–136. The American Association of Petroleum Geologists, Tulsa, Oklahoma, USA (2005)